# An Analytical Formulation of the Correlation of GNSS-R Signals

Gerardo Di Martino, *Senior Member, IEEE*, Alessio Di Simone, *Member, IEEE*, and Antonio Iodice, *Senior Member, IEEE*

***Abstract*— We present an analytical formulation of the correlation coefficient of the electromagnetic fields scattered at near-specular direction by a rough or gently undulating surface and measured at two spatially separated positions occupied by a moving receiver at slightly different times. This allows us obtaining an explicit expression of the correlation time of the received signal in terms of radar and surface parameters. This work provides a contribution to the discussion, currently ongoing in the Global Navigation Satellite System Reflectometry (GNSS-R) scientific community, about the behavior of received signal fluctuations, especially when surface profile variations are such that the scattering is neither coherent nor completely incoherent. The scattering surface is here modeled as randomly rough, and the Kirchhoff approximation (KA) or the first-order small slope approximation (SSA1) is employed to compute the scattered field. In fact, the expression of the correlation coefficient is the same for both approximations. The obtained closed-form expression shows that as the surface correlation length increases, the degree of coherence smoothly increases from the value obtained with the expression already available in the literature for very rough surfaces to a value close to unity for gently undulating surfaces. The obtained behavior of correlation time as a function of surface parameters, system resolution, and observation geometry is in agreement with numerical simulations available in the literature. In general, obtained analytical results are in agreement with the observed behavior of GNSS-R signals over flat land surfaces.**

***Index Terms*— Bistatic radar, coherence, Global Navigation Satellite System Reflectometry (GNSS-R).**

## I. Introduction

BISTATIC passive radars for remote sensing applications, exploiting transmitters of opportunity, are recently attracting much interest, due to the possibility to use light and cheap instrumentation. In this framework, Global Navigation Satellite System Reflectometry (GNSS-R), exploiting navigation satellite signals, is now a maturing technology, especially for ocean observation [1]–[7]; recently, application to land monitoring has also been proposed [8]–[13].

A parameter that plays a very important role in GNSS-R systems is the correlation time. In fact, the field scattered by a rough surface at near specular direction is the superposition of a coherent component, i.e., the mean value of the field, and an incoherent component, whose mean square modulus, i.e., whose intensity, is the field variance. As a GNSS-R receiver moves, the presence of the incoherent component causes fluctuations of the received signal around its mean value. The time scale of such fluctuations is of the order of the correlation time, and their amplitude depends on the relative weight of coherent and incoherent components, which in turn depends on the ratio of surface height standard deviation $\sigma$ and wavelength $\lambda$, and on the surface height correlation length $L$.

For ocean surfaces, at L-band, except for very calm sea, $\sigma$ is usually of the order of $\lambda$ or greater, so that the scattering is completely incoherent. In this case, the correlation time can be predicted by using an available analytical expression [1], which is substantially an application of the van Cittert-Zernike theorem [14] and is obtained by modeling the scattering surface as composed of uncorrelated point-like scatterers, similar to the approach employed to evaluate spatial decorrelation in synthetic aperture radar interferometry [15], [16]. This analytical expression of the correlation time only depends on radar parameters and observation geometry and is independent of surface roughness parameters. However, it is in reasonable agreement with GNSS-R experimental data over ocean scenes [1], [17] and with more advanced theoretical evaluations [17]–[21], that, however, require numerical integration. Only a very slight dependence on sea surface roughness is obtained in [17] for low-altitude low-velocity airborne receivers.

For land surfaces, the situation is more intricate, and it is the subject of current discussion in the GNSS-R scientific community. In particular, when flat surfaces are considered, with no large-scale topography, it is often assumed that scattering is dominated by the coherent component [9], and this may seem consistent with the fact that the received signal appears to be mainly dependent on the reflection coefficient [9], [10], [22], [23]. However, other studies show that a dominant incoherent component should be often expected in this case [11]–[13], [24]–[27]: in fact, as suggested in [12] and verified by using a LIDAR altimeter in [13], even very flat land surfaces present gentle undulations, with a large (of the order of ten to few hundred meters) horizontal scale and a vertical scale that may vary from a few centimeters to tens of centimeters. In this case, it is expected that the correlation time significantly depends on surface roughness parameters, in addition to radar ones, so that the available analytical

Manuscript received 23 February 2022; revised 16 June 2022; accepted 21 July 2022. Date of publication 25 July 2022; date of current version 9 August 2022. *(Corresponding author: Antonio Iodice.)*

The authors are with the Dipartimento di Ingegneria Elettrica e delle Tecnologie dell'Informazione, Università di Napoli Federico II, 80125 Naples, Italy (e-mail: gerardo.dimartino@unina.it; alessio.disimone@unina.it; iodice@unina.it).

Digital Object Identifier 10.1109/TGRS.2022.3193721

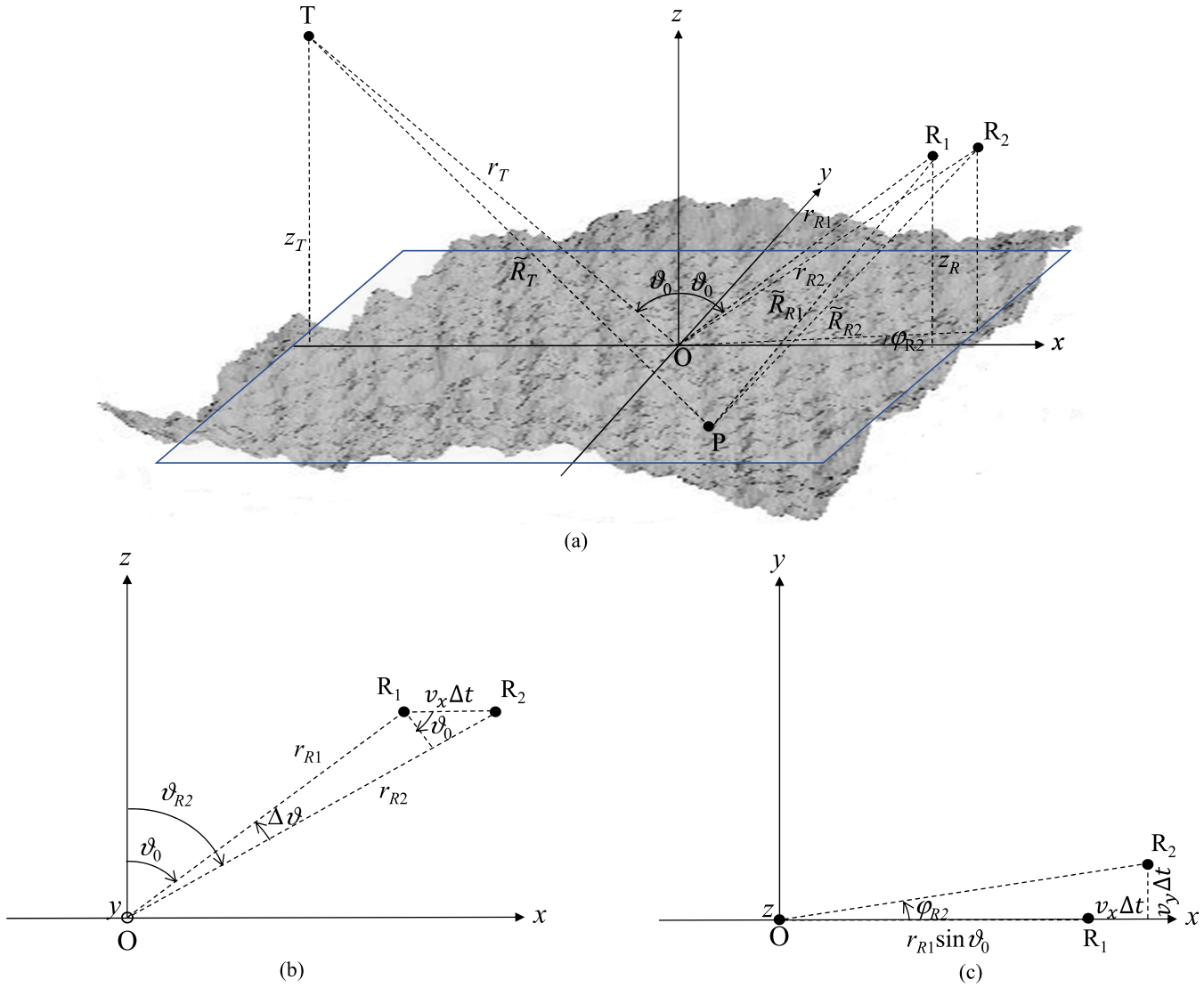


Fig. 1. Geometry of the problem: (a) 3-D view; (b) projection onto the $xz$ plane; and (c) projection onto the $xy$ plane.

expression is not useful. This is confirmed by very recent simulations presented in [12] and [28]. However, an explicit closed-form analytical formulation of the correlation time in terms of system and surface parameters is not currently available for this more general case, so that it is difficult to draw conclusions of general validity.

This work is aimed at filling this gap. In fact, here, by modeling the height deviations of the rough scattering surface as a Gaussian random process and using the Kirchhoff approximation (KA) [29], we find more general closed-form analytical expressions of the correlation and of the correlation time that also hold for slightly undulating land surfaces and explicitly depend on both system and surface parameters. The same expression is also obtained by using the first-order small slope approximation (SSA1) [30].

## II. Theory

Let us consider a rough surface $z(x, y)$, whose mean plane is the $xy$ plane, modeled as a statistically homogeneous zero-mean Gaussian random process with standard deviation $\sigma$ and normalized (to $\sigma^2$) autocorrelation function $C(\Delta x, \Delta y)$, with $\Delta x = x' - x$, $\Delta y = y' - y$, $(x, y)$, and $(x', y')$ being two generic surface points. Although it is not strictly necessary, we will assume that the surface is statistically isotropic, so that $C(\Delta x, \Delta y) = C(\Delta x^2 + \Delta y^2)$. The normalized autocorrelation function is equal to one for $\Delta x = \Delta y = 0$ and is negligible for $\Delta x$ and/or $\Delta y$ larger than the surface correlation length $L$. For wind-driven sea surfaces, $L$ is of the order of about ten times $\sigma$, whereas for gently undulating flat land surfaces, it may be much larger than that. In any case, we assume that $L$ is much smaller than the system resolution.

The geometry of the problem is depicted in Fig. 1: at time $t$, the transmitter is placed at $T \equiv (x_T, 0, z_T)$, with $x_T = -r_T \sin\vartheta_0$ and $z_T = r_T \cos\vartheta_0$; and the receiver is placed at $R_1 \equiv (x_{R1}, 0, z_R)$, with $x_{R1} = r_{R1}\sin\vartheta_0$ and $z_R = r_{R1}\cos\vartheta_0$, so that the origin $O$ is the specular point at time $t$ for the mean plane and the $xz$ plane is the vertical plane containing transmitter and receiver at time $t$. Both transmitter and receiver move, with velocities $v_T$ and $v$, respectively; but since for all spaceborne and airborne GNSS-R systems $v_T/r_T \ll v/r_{R1}$,

we can neglect the movement of the transmitter. Accordingly, at time $t + \Delta t$, we can assume that the transmitter is still in $T$, whereas the receiver has moved to the point $R_2 \equiv (x_{R2}, y_{R2}, z_R)$, with $x_{R2} = r_{R2}\sin\vartheta_{R2}\cos\varphi_{R2} = x_{R1} + v_x\Delta t$ and $y_{R2} = r_{R2}\sin\vartheta_{R2}\sin\varphi_{R2} = v_y\Delta t$, where $v_x$ and $v_y$ are the $x$- and $y$-components of the receiver velocity, so that $v = \sqrt{v_x^2 + v_y^2}$.

We assume that $v_x\Delta t \ll r_{R1}$ and $v_y\Delta t \ll r_{R1}$, so that

$$\vartheta_{R2} - \vartheta_0 = \Delta\vartheta \cong -\frac{v_x\Delta t\cos\vartheta_0}{r_{R1}}, \quad \varphi_{R2} = \Delta\varphi \cong \frac{v_y\Delta t}{r_{R1}\sin\vartheta_0}. \tag{1}$$

In addition, we suppose that the time interval $\Delta t$ is short enough to ignore surface temporal changes, both for land and sea surfaces. This assumption is of course always accurate for land, but it is also acceptable for sea surface, except for very high wind speed and low receiver velocity [31].

We consider the resolution cell that includes the specular point so that the observed area is centered in the origin and its size is related to the sensor spatial resolution. Evaluation of spatial resolution for GNSS-R systems is recalled in Appendix A, where some typical values are also provided.

By using the KA, the generic component of the scattered field at $R_1$ and $R_2$ can be written as

$$\begin{aligned} E(R_1) &= \int_{-\infty}^{\infty}\int_{-\infty}^{\infty} F(x,y)w(x,y) \\ &\quad\times \frac{\exp\{-jk[\tilde{R}_T(x,y) + \tilde{R}_{R1}(x,y)]\}}{\tilde{R}_{R1}(x,y)}dxdy \\ E(R_2) &= \int_{-\infty}^{\infty}\int_{-\infty}^{\infty} F(x,y)w(x,y) \\ &\quad\times \frac{\exp\{-jk[\tilde{R}_T(x,y) + \tilde{R}_{R2}(x,y)]\}}{\tilde{R}_{R2}(x,y)}dxdy \end{aligned} \tag{2}$$

where

1) $k = 2\pi/\lambda$ is the wavenumber;
2) $$w(x,y) = \exp\left(-\frac{x^2}{2A_x^2} - \frac{y^2}{2A_y^2}\right) \tag{3}$$ is the sensor illumination function, so that $A_x$ and $A_y$ are the semiaxes of the elliptical resolution cell that can be evaluated as shown in Appendix A;
3) $$\begin{aligned} \tilde{R}_X(x,y) &= \sqrt{(z_X - z)^2 + (x_X - x)^2 + (y_X - y)^2} \\ &= R_X(x,y)\sqrt{1 + \frac{z^2 - 2z_X z}{R_X^2(x,y)}} \\ &\cong R_X(x,y) - \frac{z_X}{R_X(x,y)}z(x,y) \end{aligned} \tag{4}$$ with $$R_X(x,y) = \sqrt{z_X^2 + (x_X - x)^2 + (y_X - y)^2} \tag{5}$$ and with the subscript $X$ that must be replaced by $T$, $R1$, or $R2$ as needed, so that, while $r_X$ are the distances of sensors from the origin, $R_X$ are their distances from the generic point $(x, y, 0)$ of the mean plane, and $\tilde{R}_X$ are their distances from the generic point $[x, y, z(x, y)]$ of the rough surface;
4) $F(x, y)$ is a slowly varying function whose expression, as shown in the following, is only of interest at $x = y = 0$: $$F(0,0) = \frac{-jkE_0\Gamma(\vartheta_0)\exp(jkr_T)\cos\vartheta_0}{2\pi} \tag{6}$$ with $E_0$ being the incident electric field at the origin and $\Gamma(\vartheta_0)$ is the reflection coefficient for the considered field component (for the *RL* circular polarization used in GNSS-R, $\Gamma(\vartheta_0)$ is the arithmetic average of Fresnel reflection coefficients at horizontal and vertical polarizations).

We explicitly note that the same formulation (2) also holds under the SSA1 [30], with a different expression of $F(x, y)$, in which the role of Fresnel reflection coefficients is played by the Bragg scattering ones [30]. However, Bragg scattering coefficients reduce to Fresnel reflection ones at specular scattering direction, i.e., at $x = y = 0$, where, therefore, the SSA1 expression of $F$ coincides with the KA one. This ensures that our results are valid under both the KA and the SSA1.

It is also important to note that the functions $F(x, y)$ and $R_X(x, y)$ are slowly spatially varying, i.e., they appreciably change only for variations of $x$ and $y$ not much smaller than $r_{R1}$. Accordingly, the variations of such functions over distances much smaller than $r_{R1}$ can be ignored, except that in the argument of the complex exponential functions in (2), where variations of $R_X(x, y)$ can be only ignored if they are much smaller than wavelength.

Finally, we note that $F(x, y)$ and $w(x, y)$ slightly change when the receiver moves from $R_1$ to $R_2$. However, if we assume that $v_x\Delta t$ and $v_y\Delta t$ are sufficiently smaller than resolution, we can ignore this change.

We want now to compute the correlation coefficient

$$\rho(\Delta t) = \frac{|\mathrm{cov}[E(R_1)E(R_2)]|}{\sqrt{\mathrm{var}[E(R_1)]\mathrm{var}[E(R_2)]}} \tag{7}$$

where

$$\begin{aligned} &\mathrm{cov}[E(R_1)E(R_2)] \\ &\quad= \left\langle [E(R_1) - \langle E(R_1)\rangle][E(R_2) - \langle E(R_2)\rangle]^*\right\rangle \\ &\quad= \left\langle E(R_1)E(R_2)^*\right\rangle - \langle E(R_1)\rangle\langle E(R_2)\rangle^* \end{aligned} \tag{8}$$

$$\begin{aligned} \mathrm{var}\left[E\left(R_{1,2}\right)\right] &= \left\langle \left|E\left(R_{1,2}\right) - \left\langle E\left(R_{1,2}\right)\right\rangle\right|^2\right\rangle \\ &= \left\langle \left|E\left(R_{1,2}\right)\right|^2\right\rangle - \left|\left\langle E\left(R_{1,2}\right)\right\rangle\right|^2 \end{aligned} \tag{9}$$

and the symbol $\langle\cdot\rangle$ indicates the statistical mean (i.e., the ensemble average). The correlation coefficient is obviously unitary for $\Delta t = 0$, and the correlation time $\tau$ is conventionally the value of $\Delta t$ such that $\rho$ has decreased to the value $1/e$.

By using (2) in (9), we get (10), as shown at the bottom of the next page, where

$$u_{z1,2}(x,y) = \frac{z_T}{R_T(x,y)} + \frac{z_R}{R_{R1,2}(x,y)}. \tag{11}$$

Let us now focus on the following function that appears in (10):

$$f(x,y,x',y') = \langle \exp\{jk[u_{z1}(x,y)z(x,y) - u_{z2}(x',y')z(x',y')]\}\rangle - \langle \exp\{jk[u_{z1}(x,y)z(x,y)]\}\rangle \times \langle \exp\{-jk[u_{z2}(x',y')z(x',y')]\}\rangle.$$

The statistical means that appear in this expression are the characteristic functions [32] of Gaussian random variables so that they can be readily computed, see Appendix D

$$\begin{aligned} f(x,y,x',y') &= \exp\left\{-\frac{k^2\sigma^2}{2}\left[u_{z1}^2(x,y)+u_{z2}^2(x'y') - 2u_{z1}(x,y)u_{z2}(x'y')C(\Delta x,\Delta y)\right]\right\} - \exp\left\{-\frac{k^2\sigma^2}{2}\left[u_{z1}^2(x,y)+u_{z2}^2(x'y')\right]\right\} \\ &= \exp\left\{-\frac{k^2\sigma^2}{2}\left[u_{z1}(x,y)-u_{z2}(x'y')\right]^2\right\} \times \left[\exp\{-k^2\sigma^2 u_{z1}(x,y)u_{z2}(x',y')[1-C(\Delta x,\Delta y)]\} - \exp\{-k^2\sigma^2 u_{z1}(x,y)u_{z2}(x'y')\}\right]. \end{aligned} \quad (12)$$

If $k^2\sigma^2 \gg 1$ (i.e., if $\sigma$ is greater than about $\lambda/2$, which for a frequency of 1.5 GHz corresponds to $\sigma > 10$ cm), then $f$ is appreciably different from zero only for $\Delta x$ and $\Delta y$ much smaller than $L$, where $C(\Delta x, \Delta y) \cong 1$. For smaller values of $k\sigma$, $f$ is appreciably different from zero only for $\Delta x$ and $\Delta y$ not larger than $L$, where $C(\Delta x, \Delta y)$ is not negligible. Therefore, the integrand of (10) is appreciably different from zero only for $|x - x'|$ and $|y - y'|$ smaller or much smaller than $L$, and in the first exponential of (10), we can let

$$\begin{aligned} R_T(x,y) + R_{R1}(x,y) - R_T(x'y') - R_{R2}(x'y') &= R_T(x,y) + R_{R1}(x,y) - R_T(x'y') - R_{R1}(x'y') + R_{R1}(x'y') - R_{R2}(x'y') \\ &\cong -u_x(x,y)\Delta x - u_y(x,y)\Delta y + R_{R1}(x,y) - R_{R2}(x,y) \end{aligned} \quad (13)$$

where [also recalling that $x_T < 0$, see Fig. 1(a)]

$$u_x(x,y) = \frac{\partial(R_T + R_{R1})}{\partial x} = \frac{x + |x_T|}{R_T(x,y)} + \frac{x - x_{R1}}{R_{R1}(x,y)}$$
$$u_y(x,y) = \frac{\partial(R_T + R_{R1})}{\partial y} = y\left(\frac{1}{R_T(x,y)} + \frac{1}{R_{R1}(x,y)}\right). \quad (14)$$

Considering that $L$ is much smaller than resolution, which in turns is usually much smaller than the receiver distance $r_{R1}$ (see Appendix A), elsewhere in (10) and (12), apart from $C(\Delta x, \Delta y)$, we can assume $x = x'$, $y = y'$. Therefore, (12) can be rewritten as

$$f(x,y,x',y') = \exp\left\{-\frac{k^2\sigma^2}{2}\left[u_{z1}(x,y) - u_{z2}(x,y)\right]^2\right\} \times \left[\exp\{-k^2\sigma^2 u_z^2(x,y)[1 - C(\Delta x,\Delta y)]\} - \exp\{-k^2\sigma^2 u_z^2(x,y)\}\right] \quad (15)$$

where we have set $u_z(x,y) = (u_{z1}(x,y)u_{z2}(x,y))^{1/2}$.

Note that in (13) we have set $R_{R1}(x',y') - R_{R2}(x',y') \cong R_{R1}(x,y) - R_{R2}(x,y)$. It can be shown that the corresponding error is of the order of $(v\Delta t/r_{R1})$ times the distance from $(x,y)$ to $(x',y')$. Therefore, our approximation holds if $(v\Delta t/r_{R1})L$ does not exceed $\lambda$. For example, for a typical spaceborne GNSS-R system, $L$ cannot exceed few hundred meters.

In Appendix B, we show that if the surface autocorrelation function is Gaussian, i.e., if

$$C(\Delta x, \Delta y) = \exp\left(-\frac{\Delta x^2 + \Delta y^2}{L^2}\right) \quad (16)$$

then for any value of $\sigma$, the function $f$ can be approximated as

$$f(x,y,x',y') \cong \exp\left\{-\frac{k^2\sigma^2}{2}\left[u_{z1}(x,y) - u_{z2}(x,y)\right]^2\right\} \times a^2(x,y)\exp\left\{-\frac{k^2\sigma^2 u_z^2(x,y)}{L^2 a^2(x,y)}\left[\Delta x^2 + \Delta y^2\right]\right\} \quad (17)$$

where

$$a(x,y) = \sqrt{1 - \exp\{-k^2\sigma^2 u_z^2(x,y)\}}. \quad (18)$$

If $k^2\sigma^2 \gg 1$, then $a(x,y) \cong 1$ and

$$f(x,y,x',y') \cong \exp\left\{-\frac{k^2\sigma^2}{2}\left[u_{z1}(x,y) - u_{z2}(x,y)\right]^2\right\} \times \exp\left\{-\frac{k^2\sigma^2 u_z^2(x,y)}{L^2}\left[\Delta x^2 + \Delta y^2\right]\right\}. \quad (19)$$

As also shown in Appendix B, for $k^2\sigma^2 \gg 1$, (19) holds for any regular autocorrelation function, provided that, for non-Gaussian correlation function, $L^2$ is replaced by $2/|C''(0)|$.

By using (13) and (17) in (10), we have (20), as shown at the bottom of the next page.

$$\begin{aligned} \operatorname{cov}[E(R_1)E(R_2)] &\cong \int_{-\infty}^{\infty}\int_{-\infty}^{\infty}\int_{-\infty}^{\infty}\int_{-\infty}^{\infty} \frac{\exp\{-jk[R_T(x,y) + R_{R1}(x,y) - R_T(x',y') - R_{R2}(x',y']\}}{R_{R1}(x,y)R_{R2}(x',y'} \\ &\cdot F(x,y)w(x,y)F^*(x',y')w(x',y') \\ &\times \left[\langle \exp\{jk[u_{z1}(x,y)z(x,y) - u_{z2}(x',y')z(x',y')]\}\rangle \right. \\ &\quad \left. - \langle \exp\{jk[u_{z1}(x,y)z(x,y)]\}\rangle\langle \exp\{-jk[u_{z2}(x',y')z(x',y')]\}\rangle\right] \\ &\times dxdydx'dy' \end{aligned} \quad (10)$$

The integrals over $\Delta x$ and $\Delta y$ in (20) are the Fourier transform (FT) of Gaussian functions, see Appendix D, so that they can be readily computed (21), as shown at the bottom of the page.

The sensor illumination function $w$ in (21) is peaked around the origin and is appreciably different from zero only in the resolution cell of area $\pi A_x A_y$. In addition, since $u_x(0,0) = (|x_T|/r_T) - (x_{R1}/r_{R1}) = 0$ and $u_y(0,0) = 0$, also the last exponential in (21) is peaked around the origin, and the area in which it is appreciably different from zero (the so-called "glistening area," i.e., the ground area appreciably contributing to the field scattered toward the receiver) can be evaluated by expanding the exponent around the origin: as shown in Appendix C

$$\exp\left\{-\frac{1}{2}\frac{u_x^2(x,y)+u_y^2(x,y)}{2\frac{\sigma^2 u_z^2(x,y)}{L^2a^2(x,y)}}\right\} \cong \exp\left(-\frac{x^2}{G_x^2}-\frac{y^2}{G_y^2}\right) \quad (22)$$

where

$$G_x = \frac{4\sigma}{a_0 L\cos\vartheta_0}\frac{r_T r_{R1}}{r_T + r_{R1}} \cong \frac{4\sigma r_{R1}}{a_0 L\cos\vartheta_0}$$
$$G_y = \frac{4\sigma\cos\vartheta_0}{a_0 L}\frac{r_T r_{R1}}{r_T + r_{R1}} \cong \frac{4\sigma\cos\vartheta_0 r_{R1}}{a_0 L} \quad (23)$$

are the $x$ and $y$ sizes of the glistening area, with

$$a_0 = a(0,0) = \sqrt{1-\exp\{-4k^2\sigma^2\cos^2\vartheta_0\}}$$
$$u_z(0,0) = \sqrt{2\cos\vartheta_0(\cos\vartheta_0+\cos\vartheta_{R2})} \cong 2\cos\vartheta_0 \quad (24)$$

and we have used the fact that for all GNSS-R systems $r_T \gg r_{R1}$.

Since the resolution is usually much smaller than $r_{R1}$, see Appendix A, in the resolution cell, the argument of the first exponential in (21) can also be approximated by expanding it around the origin

$$R_{R1}(x,y) - R_{R2}(x,y) \cong r_{R1} - r_{R2} + \eta_x x + \eta_y y \quad (25)$$

where

$$\eta_x = \left.\frac{\partial(R_{R1}-R_{R2})}{\partial x}\right|_{\substack{x=0\\y=0}} = -\frac{x_{R1}}{r_{R1}} + \frac{x_{R2}}{r_{R2}}$$
$$= -\sin\vartheta_0 + \sin\vartheta_{R2}\cos\varphi_{R2} \cong \cos\vartheta_0\Delta\vartheta \cong -\frac{\cos^2\vartheta_0 v_x\Delta t}{r_{R1}}$$
$$\eta_y = \left.\frac{\partial(R_{R1}-R_{R2})}{\partial y}\right|_{\substack{x=0\\y=0}} = \frac{y_{R2}}{r_{R2}} = \sin\vartheta_{R2}\sin\varphi_{R2}$$
$$\cong \sin\vartheta_0\Delta\varphi \cong \frac{v_y\Delta t}{r_{R1}} \quad (26)$$

and all other functions in (21) can be assumed approximately constant in the resolution cell and equal to their value in the origin

$$F(x,y) \cong F(0,0)$$
$$u_{z1}(x,y) - u_{z2}(x,y) \cong \cos\vartheta_0 - \cos\vartheta_{R2} \cong \sin\vartheta_0\Delta\vartheta \cong \frac{\sin\vartheta_0\cos\vartheta_0 v_x\Delta t}{r_{R1}}$$
$$a(x,y) \cong a_0, u_z(x,y) \cong u_z(0,0) \cong 2\cos\vartheta_0 \quad (27)$$

where $F(0,0)$ and $a_0$ are given in (6) and (24), respectively.

By using (22)–(27) and (3) in (21), we get

$$\mathrm{cov}[E(R_1)E(R_2)] \cong \frac{a_0^2|E_0|^2|\Gamma|^2}{8\pi r_{R1}r_{R2}}\frac{a_0^2L^2}{2\sigma^2}\exp[-jk(r_{R1}-r_{R2})] \times \exp\left\{-\frac{1}{2}\left[\frac{k\sigma\sin\vartheta_0\cos\vartheta_0 v_x\Delta t}{r_{R1}}\right]^2\right\} \times \int_{-\infty}^{\infty}\exp\left\{-\left(\frac{1}{A_x^2}+\frac{1}{G_x^2}\right)x^2\right\}\exp[-jk\eta_x x]dx$$

$$\mathrm{cov}[E(R_1)E(R_2)] \cong \int_{-\infty}^{\infty}\int_{-\infty}^{\infty}\frac{|F(x,y)|^2 w^2(x,y)\exp\{-jk[R_{R1}(x,y)-R_{R2}(x,y)]\}}{R_{R1}(x,y)R_{R2}(x,y)} \times \exp\left\{-\frac{k^2\sigma^2}{2}\left[u_{z1}(x,y)-u_{z2}(x,y)\right]^2\right\}a^2(x,y) \times \int_{-\infty}^{\infty}\exp[jku_x(x,y)\Delta x]\exp\left[-\frac{k^2\sigma^2u_z^2(x,y)\Delta x^2}{L^2a^2(x,y)}\right]d\Delta x \times \int_{-\infty}^{\infty}\exp\left[jku_y(x,y)\Delta y\right]\exp\left[-\frac{k^2\sigma^2u_z^2(x,y)\Delta y^2}{L^2a^2(x,y)}\right]d\Delta y dx dy. \quad (20)$$

$$\mathrm{cov}[E(R_1)E(R_2)] \cong \int_{-\infty}^{\infty}\int_{-\infty}^{\infty}\frac{|F(x,y)|^2 w^2(x,y)\exp\{-jk[R_{R1}(x,y)-R_{R2}(x,y)]\}}{R_{R1}(x,y)R_{R2}(x,y)}\exp\left\{-\frac{k^2\sigma^2}{2}\left[u_{z1}(x,y)-u_{z2}(x,y)\right]^2\right\} \times \frac{2\pi L^2a^4(x,y)}{k^2 2\sigma^2u_z^2(x,y)}\exp\left\{-\frac{1}{2}\frac{u_x^2(x,y)+u_y^2(x,y)}{2\frac{\sigma^2u_z^2(x,y)}{L^2a^2(x,y)}}\right\}dxdy. \quad (21)$$

$$\times \int_{-\infty}^{\infty} \exp\left\{-\left(\frac{1}{A_y^2}+\frac{1}{G_y^2}\right)y^2\right\}\exp\left[-jk\eta_y y\right]dy. \tag{28}$$

The integrals over $x$ and $y$ in (28) are again the FT of Gaussian functions, see Appendix D, so that they can be readily computed (29), as shown at the bottom of the next page, where

$$W_{x,y} = \frac{A_{x,y}G_{x,y}}{\sqrt{A_{x,y}^2+G_{x,y}^2}} \tag{30}$$

and we have used (26).

The field variances are easily deduced from (29) by setting $\Delta t = 0$, and $r_{R2} \to r_{R1}$ for $E(R_1)$ and $r_{R1} \to r_{R2}$ for $E(R_2)$

$$\mathrm{var}\left[E\left(R_{1,2}\right)\right] \cong \frac{a_0^2|E_0|^2|\Gamma|^2}{8\pi r_{R1,2}^2}\frac{a_0^2L^2}{2\sigma^2}\pi W_x W_y. \tag{31}$$

By replacing (29) and (31) in (7) and noting that $\sigma \ll W_x$, we finally get

$$\rho(\Delta t) \cong \exp\left\{-\frac{k^2\Delta t^2\left[W_x^2\cos^4\vartheta_0 v_x^2 + W_y^2 v_y^2\right]}{4r_{R1}^2}\right\} \tag{32}$$

and

$$\tau \cong \frac{2r_{R1}}{k\sqrt{W_x^2\cos^4\vartheta_0 v_x^2 + W_y^2 v_y^2}} = \frac{\lambda r_{R1}}{\pi\sqrt{W_x^2\cos^4\vartheta_0 v_x^2 + W_y^2 v_y^2}}. \tag{33}$$

Equations (31)–(33), together with the well-known mean field expression

$$\left|\left\langle E\left(R_{1,2}\right)\right\rangle\right| \cong \frac{|E_0||\Gamma|r_T}{r_T + r_{R1,2}}\exp\left\{-2k^2\sigma^2\cos^2\vartheta_0\right\} \tag{34}$$

that holds if the first Fresnel zone is included in the resolution cell (a more accurate expression, accounting for Earth's surface curvature, is available in [33]), allow to completely characterize the field fluctuations at the receiver.

It is useful to summarize here the assumptions that we made to obtain (29)–(33): we assumed that $v_x\Delta t$, $v_y\Delta t$, and $L$ are much smaller than resolution, and that resolution is much smaller than the receiver distance $r_{R1}$. In Appendix A, we show that these conditions are usually satisfied for spaceborne and airborne GNSS-R systems, the most critical situation being incidence at low grazing angle and, above all, a low-altitude airborne receiver, for which resolution is not much smaller than the receiver distance. However, in Section IV, we show that even in this last critical case, our analytical formulation is in very good agreement with numerical simulations available in the literature. It is finally worth recalling that SSA1 holds for small values of $\sigma/L$ (not exceeding about 0.15 [29], [30]). This condition is often satisfied by sea surfaces, for which SSA1 is widely used, and it is always satisfied by gently undulating surfaces.

## III. Discussion

The obtained closed-form expressions of correlation coefficient and correlation time depend on the parameters $W_{x,y}$, which are a combination of system resolutions $A_{x,y}$ and sizes of the glistening area $G_{x,y}$. In particular, see (30), $W_{x,y}$ is approximately equal to the smaller of $A_{x,y}$ and $G_{x,y}$. Therefore, if $A_{x,y} < G_{x,y}$, i.e., the surface area contributing to the received signal is limited by the system resolution, then $W_{x,y} \cong A_{x,y}$; conversely, if $G_{x,y} < A_{x,y}$, i.e., the surface area contributing to the received signal is limited by the glistening area size, then $W_{x,y} \cong G_{x,y}$.

As illustrated in Appendix A, for wind-driven sea surfaces and land surfaces with significant large-scale topography ($\sigma/L \sim 0.1$, $a_0 \cong 1$), we have usually (except for low-altitude low-velocity airborne receivers) $A_{x,y} < G_{x,y}$ so that $W_{x,y} \cong A_{x,y}$. Accordingly, (31)–(33) can be rewritten as

$$\mathrm{var}\left[E\left(R_{1,2}\right)\right] \cong \frac{a_0^2|E_0|^2|\Gamma|^2}{8\pi r_{R1,2}^2}\frac{a_0^2L^2}{2\sigma^2}\pi A_x A_y \tag{35}$$

$$\rho(\Delta t) \cong \exp\left\{-\frac{k^2\Delta t^2\left[A_x^2\cos^4\vartheta_0 v_x^2 + A_y^2 v_y^2\right]}{4r_{R1}^2}\right\} \tag{36}$$

and

$$\tau \cong \frac{2r_{R1}}{k\sqrt{A_x^2\cos^4\vartheta_0 v_x^2 + A_y^2 v_y^2}} = \frac{\lambda r_{R1}}{\pi\sqrt{A_x^2\cos^4\vartheta_0 v_x^2 + A_y^2 v_y^2}}. \tag{37}$$

In this case, our result for the correlation time is in agreement with the classical one [1]. By using the expressions of the pulse-limited system resolutions, see (45), we get

$$\tau \cong \frac{\lambda}{\pi}\sqrt{\frac{r_{R1}B}{c\left(\cos^2\vartheta_0 v_x^2 + v_y^2\right)}}. \tag{38}$$

In conclusion, it turns out that if $A_{x,y} < G_{x,y}$, the correlation time is only dependent on system parameters and is independent of surface ones, whereas the field variance significantly depends also on surface parameters. All this is in full agreement with what is observed in real GNSS-R data over the ocean [1], [2] and over land surfaces with significant large-scale topography [8], [34].

Conversely, for gently undulating flat land surfaces, $\sigma/(a_0L)$ may be of the order of 0.01 or even 0.001 (for instance, for $\sigma = 0.1$ m and $L = 100$ m), so that, as shown in Appendix A, usually $G_{x,y} < A_{x,y}$, and $W_{x,y} \cong G_{x,y}$. Accordingly, (31)–(33) can be rewritten as

$$\mathrm{var}\left[E\left(R_{1,2}\right)\right] \cong \frac{a_0^2|E_0|^2|\Gamma|^2}{8\pi r_{R1,2}^2}\frac{a_0^2L^2}{2\sigma^2}\pi G_x G_y \cong \frac{a_0^2|E_0|^2|\Gamma|^2 r_T^2}{\left(r_T + r_{R1,2}\right)^2} \tag{39}$$

$$\rho(\Delta t) \cong \exp\left\{-\frac{k^2\Delta t^2\left[G_x^2\cos^4\vartheta_0 v_x^2 + G_y^2 v_y^2\right]}{4r_{R1}^2}\right\} \cong \exp\left\{-\frac{4k^2\Delta t^2\sigma^2\cos^2\vartheta_0 v^2}{a_0^2L^2}\right\} \tag{40}$$

TABLE I
RECEIVERS' PARAMETERS

| Parameter | | Value | | |
|---|---|---|---|---|
| | | *Low-altitude airborne* | *High-altitude airborne* | *Spaceborne* |
| *Wavelength* | $\lambda$ | 19 cm | 19 cm | 19 cm |
| *Sensor height* | $z_R$ | 100 m | 10 km | 540 km |
| *Incidence angle* | $\vartheta_0$ | 15 deg | 30 deg | 30 deg |
| *Signal bandwidth* | $B$ | 1 MHz | 1 MHz | 1 MHz |
| *Sensor velocity* | | | | |
| *along x* | $v_x$ | 60 m/s | 250 m/s | 7 km/s |
| *along y* | $v_y$ | 0 | 0 | 0 |
| *Semi-resolution* | | | | |
| *along x* | $A_x$ | 130 m | 585 m | 11280 m |
| *along y* | $A_y$ | 130 m | 1860 m | 13680 m |

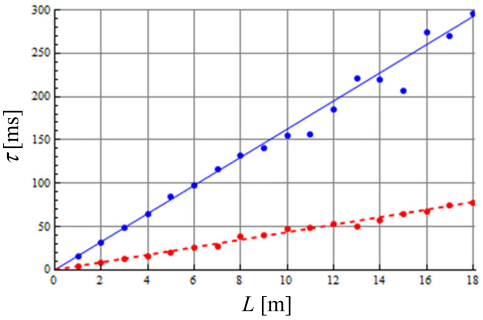


Fig. 2. Correlation time $\tau$ versus correlation length $L$, computed via (32) (lines) and via numerical simulations of [12] (dots), for $\sigma = 0.5$ cm (blue solid line and blue dots) and $\sigma = 6$ cm (red dashed line and red dots). System parameters are those of the very-low-altitude airborne receiver, first column of Table I.

and

$$\tau \cong \frac{\lambda r_{R1}}{\pi\sqrt{G_x^2\cos^4\vartheta_0 v_x^2 + G_y^2 v_y^2}} \cong \frac{\lambda a_0 L}{4\pi\sigma v\cos\vartheta_0}. \tag{41}$$

Therefore, in this case, the correlation time is also dependent on surface parameters, and in particular, it linearly increases with $L$: even when $\sigma$ is of the order of $\lambda$ or larger, so that the incoherent component dominates the scattered field, the received signal may remain correlated for a rather long time, provided that $L$ is sufficiently large (i.e., undulations are sufficiently gentle).

We note that for large $\sigma$ (at least of the order of $\lambda$), we have $a_0 \cong 1$ and the correlation time dependence on surface parameters is only in terms of the ratio $\sigma/L$, i.e., of the root mean square (rms) surface slope. The other limiting case is for $\sigma$ small compared to $\lambda$. In this case, $a_0 \cong 2k\sigma\cos\vartheta_0$ and (41) becomes

$$\tau \cong \frac{L}{v} \tag{42}$$

i.e., in this limiting case, the correlation time is equal to the time needed by the receiver to travel a distance equal to the surface correlation length.

Finally, it is interesting to note that using (34) and (39), we get the following expression of the received field mean intensity:

$$\left\langle \left|E\left(R_{1,2}\right)\right|^2 \right\rangle = \mathrm{var}\left[E\left(R_{1,2}\right)\right] + \left|\left\langle E\left(R_{1,2}\right)\right\rangle\right|^2 \cong \frac{|E_0|^2|\Gamma|^2 r_T^2}{\left(r_T + r_{R1,2}\right)^2} \tag{43}$$

i.e., it coincides with the intensity of the field reflected by a smooth surface, regardless of the surface undulations. This may explain why over flat gently undulating land surfaces although the field may be dominated by the incoherent component, after incoherent integration, the signal turns out to be mainly sensitive to soil moisture (through the reflection coefficient) and only very slightly depending on the surface roughness, as experimentally reported [9], [10], [22], [23].

In conclusion, it turns out that if $G_{x,y} < A_{x,y}$, the correlation time depends on both system and surface parameters, whereas the overall average field intensity is only dependent on system parameters and soil permittivity and is independent of surface roughness.

## IV. NUMERICAL RESULTS

In this section, we first of all compare the results of our closed-form formulation with those recently obtained via a numerical method in [12], and then, we show meaningful results obtained by using system parameters of actual GNSS-R receivers.

Let us then first consider the system parameters of the very-low-altitude airborne GNSS-R receiver reported in the first column of Table I. These are the same parameters considered in [12]: in that work, the integrals in (2) were computed numerically, and correlation coefficient and intensities of coherent and incoherent components were evaluated via Monte Carlo simulation, by generating several realizations of a random surface profile with Gaussian probability density function and Gaussian autocorrelation function (or simulating a single very long acquisition, see [12] for details). This allows avoiding the approximations we made to obtain our closed-form formulation, but it has a high computational cost. In addition, results obtained with the numerical method of [12] cannot be easily generalized to other realistic airborne and spaceborne

$$\mathrm{cov}[E(R_1)E(R_2)] \cong \frac{a_0^2|E_0|^2|\Gamma|^2}{8\pi r_{R1}r_{R2}}\frac{a_0^2L^2}{2\sigma^2}\exp[-jk(r_{R1}-r_{R2})]\pi W_x W_y \times \exp\left\{-\frac{k^2\Delta t^2\left[\left(W_x^2\cos^2\vartheta_0 + \sigma^2\sin^2\vartheta_0\right)\cos^2\vartheta_0 v_x^2 + W_y^2 v_y^2\right]}{4r_{R1}^2}\right\} \tag{29}$$

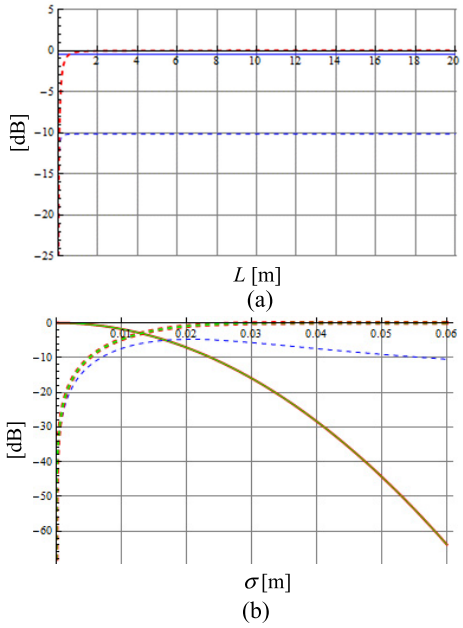


Fig. 3. Intensities of the coherent (solid lines) and incoherent (dashed lines) components: (a) as a function of $L$ for $\sigma = 0.5$ cm (blue lines) and $\sigma = 6$ cm (red line, negligible coherent component) and (b) as a function of $\sigma$, for $L = 0.06$ m (blue lines), $L = 6$ m (red lines), and $L = 20$ m (green lines). All intensities are normalized to the intensity of the field reflected by a smooth plane. System parameters are those of the very-low-altitude airborne receiver, first column of Table I.

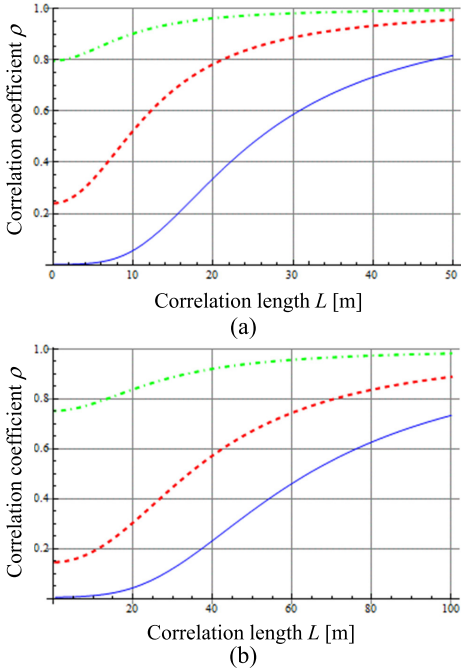


Fig. 4. Correlation coefficient $\rho$ versus correlation length $L$, with $\sigma = 10$ cm: (a) for a high-altitude airborne receiver with $\Delta t = 16$ ms (blue solid line), $\Delta t = 8$ ms (red dashed line), and $\Delta t = 3.2$ ms (green dotted-dashed line) and (b) for a spaceborne receiver with $\Delta t = 1.43$ ms (blue solid line), $\Delta t = 0.93$ ms (red dashed line), and $\Delta t = 0.36$ ms (green dotted-dashed line). System parameters are reported in the second and third columns of Table I.

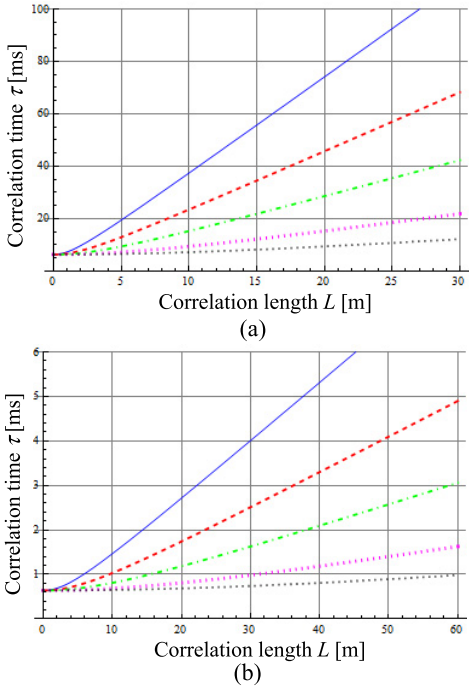


Fig. 5. Correlation time $\tau$ versus correlation length $L$: (a) for a high-altitude airborne receiver and (b) for a spaceborne receiver, with $\sigma = 1$ cm (blue solid line), $\sigma = 3$ cm (red dashed line), $\sigma = 5$ cm (green dotted-dashed line), $\sigma = 10$ cm (magenta dotted line), and $\sigma = 20$ cm (black dotted line). System parameters are reported in the second and third columns of Table I.

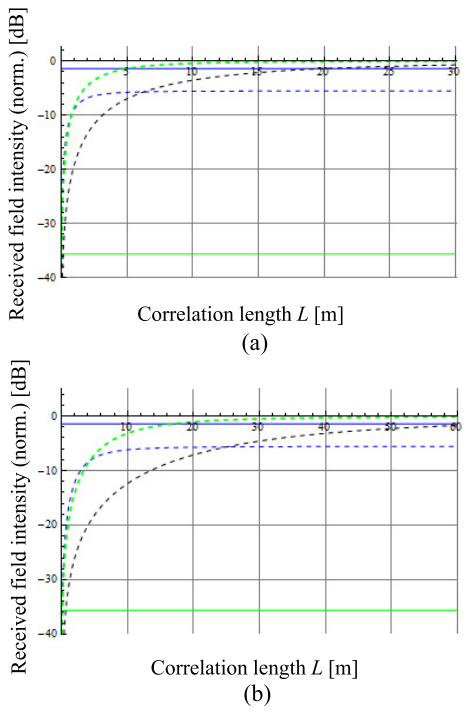


Fig. 6. Intensities of the coherent (solid lines) and incoherent (dashed lines) components: (a) for a high-altitude airborne receiver and (b) for a spaceborne receiver, with $\sigma = 1$ cm (blue lines), $\sigma = 5$ cm (green lines), and $\sigma = 20$ cm (black line, negligible coherent component). System parameters are reported in the second and third columns of Table I.

receivers, and they do not allow for a straightforward investigation of the role of system and scene parameters.

In Fig. 2, we show the correlation time $\tau$ as a function of the correlation length $L$ for two values of $\sigma$, computed by using (33) (lines) and compared to those obtained in [12] (dots, see [12, Fig. 9]). Fig. 2 shows that our results are in excellent agreement with numerical simulations of [12].

In Fig. 3, we plot the intensities of the incoherent component, computed via our formulation (31), and of the coherent component, computed as the square of (34). We note that for

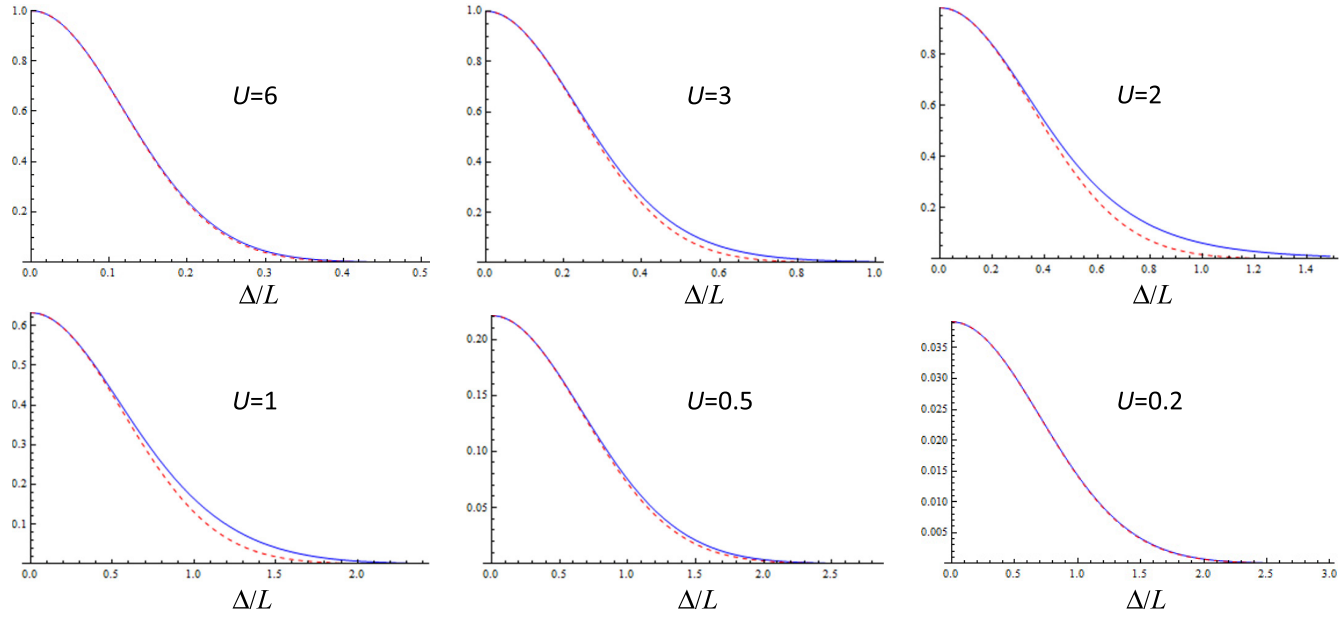


Fig. 7. Plots of the functions $g$ (blue solid lines) and $\tilde{g}$ (red dashed lines) versus $\Delta/L$ for different values of $U$.

TABLE II

RESOLUTIONS AND GLISTENING AREA SIZES. FOR ALL SYSTEMS, WAVELENGTH IS 19 cm AND SIGNAL BANDWIDTH IS 1 MHz

| **Parameter** | | **Value** | | | | | | | | |
|---|---|---|---|---|---|---|---|---|---|---|
| | | *Low-altitude airborne* | | | *High-altitude airborne* | | | *Spaceborne* | | |
| | | $\vartheta_0$=15° | $\vartheta_0$=30° | $\vartheta_0$=60° | $\vartheta_0$=15° | $\vartheta_0$=30° | $\vartheta_0$=60° | $\vartheta_0$=15° | $\vartheta_0$=30° | $\vartheta_0$=60° |
| *Sensor height* | $z_R$ | 100 m | | | 10 km | | | 540 km | | |
| *Sensor velocity* | $v_x$ | 60 m/s | | | 250 m/s | | | 7 km/s | | |
| | $v_y$ | 0 | | | 0 | | | 0 | | |
| *Coherent integration time* | $t_{ci}$ | NA | | | 10 ms | | | 1 ms | | |
| *Beam-limited* | $A_{xa}$ | 130 m | 162 m | 485 m | $>>A_{xp}$ | $>>A_{xp}$ | $>>A_{xp}$ | $>>A_{xp}$ | $>>A_{xp}$ | $>>A_{xp}$ |
| *semi-resolution* | $A_{ya}$ | 130 m | 145 m | 250 m | $>>A_{yp}$ | $>>A_{yp}$ | $>>A_{yp}$ | $>>A_{yp}$ | $>>A_{yp}$ | $>>A_{yp}$ |
| *Pulse-limited* | $A_{xp}$ | 182 m | 215 m | 490 m | 1825 m | 2150 m | 5000 m | 13410 m | 15790 m | 36 km |
| *semi-resolution* | $A_{yp}$ | 176 m | 186 m | 245 m | 1762 m | 1860 m | 2500 m | 12950 m | 13680 m | 18 km |
| *Doppler-limited* | $A_{xD}$ | NA | NA | NA | 421 m | 585 m | 3040 m | 8130 m | 11280 m | 58 km |
| *semi-resolution* | $A_{yD}$ | NA | NA | NA | $>>A_{yp}$ | $>>A_{yp}$ | $>>A_{yp}$ | $>>A_{yp}$ | $>>A_{yp}$ | $>>A_{yp}$ |
| *Glistening area* | $G_x$ | 42.9 m | 53.3 m | 160 m | 4287 m | 5333 m | 16000 m | 231 km | 288 km | 864 km |
| $\sigma/(a_0L)$=0.1 | $G_y$ | 40.0 m | 40.0 m | 40.0 m | 4000 m | 4000 m | 4000 m | 216 km | 216 km | 216 km |
| *Glistening area* | $G_x$ | 2.14 m | 2.66 m | 8.00 m | 214 m | 266 m | 800 m | 11550 m | 14400 m | 43.2 km |
| $\sigma/(a_0L)$=0.005 | $G_y$ | 2.00 m | 2.00 m | 2.00 m | 200 m | 200 m | 200 m | 10800 m | 10800 m | 10800 m |

this very-low-altitude receiver, the glistening area becomes smaller than resolution already for $L$ equal to about 0.5 m, and for higher values of $L$ (31) is well-approximated by (39), so that the intensity of the incoherent component becomes independent of $L$. We also note that the intensity of coherent component is always independent of $L$, according to the classical formulation of (34). These results can be compared with incoherent and coherent intensities obtained via numerical simulations for observation times much longer than the correlation time, so that our Fig. 3(a) and (b) can be compared with Figs. 8(a) and 6(a) of [12], respectively. It can be noted that the intensities of incoherent components evaluated via our formulation (31) are again in excellent agreement with numerical simulations of [12]. And the intensities of coherent components evaluated via the classical formulation of (34) are also in very good agreement with numerical simulations, except for very low values of such intensities.

For the remaining numerical examples of results obtained by our analytical formulation, we consider the system parameters of the high-altitude airborne and spaceborne receivers, reported in the second and third columns of Table I, respectively. The former is GOLD-RTR that has been used in more than 40 flights over oceans, lakes, and land [35]; the latter is SGR-ReSi that has been adopted in past and current spaceborne GNSS-R missions, e.g., TechDemoSat-1 and CYGNSS [36].

In Fig. 4, we plot the correlation coefficient, computed by using (32), as a function of $L$ for $\sigma = 10$ cm and for different time lags. Fig. 4 shows that as the surface correlation length increases, the correlation coefficient smoothly increases from the value obtained with the expression already available in [1] for uncorrelated scatterers to a value close to unity for gently undulating surfaces. This transition occurs at smaller values of $L$ for the airborne system.

Fig. 5 shows the correlation time, computed by using (33), as a function of $L$ for several values of $\sigma$. Again, as the surface correlation length increases, the correlation time initially coincides with the value obtained via (37), i.e., the

already available expression (namely, 6.7 and 0.62 ms for the airborne and spaceborne systems, respectively), and then, it starts increasing. This increase is faster for lower $\sigma$, and it starts at lower values of $L$ for lower $\sigma$. In fact, the transition between the two identified regimes depends on $G_{x,y}$ and, hence, on the ratio of $\sigma$ and $L$, see (23). The values of the correlation time are higher for the airborne receiver.

Finally, in Fig. 6, we plot the intensities of the incoherent component, computed via our formulation (31), and of the coherent component, computed as the square of (34). The general behavior is similar to the one observed in Fig. 3; however, for these higher receiver altitudes, the values of the surface correlation length for which (31) starts to be well-approximated by (39) are higher.

## V. Conclusion

We have presented an analytical formulation of the temporal correlation of GNSS-R signals reflected off the Earth' surface. The proposed expressions have been derived under either the KA (without subsequent approximations, e.g., geometrical optics) or the SSA1 theoretical frameworks, which, indeed, both lead to the same formulation of the correlation coefficient. The scattering surface height has been modeled as a random rough Gaussian process and no limitations on both height standard deviation and correlation length have been imposed, apart from those required by the adopted scattering models, and provided that they are much smaller than resolution. Accordingly, most roughness regimes typically sensed by GNSS-R and ranging from very rough surfaces, such as wind-driven sea surfaces, to very smooth surfaces, such as gently undulating land surfaces, can be analyzed with the proposed theoretical approach. The final closed-form general expressions of the correlation coefficient and of the correlation time hold for any surface autocorrelation function when $k\sigma$ is large, and for Gaussian surface autocorrelation when $k\sigma$ is not large. Extensions of the approach to non-Gaussian autocorrelation functions even for small $k\sigma$, as well as to fractal-based surface models [37], are the subject of ongoing research.

From the general formulation, specific simplified expressions of the correlation time have been obtained in the two extreme roughness regimes, namely, very rough and gently undulating surfaces. In the former case, the formulation leads to an already available expression, where the correlation time only depends on system parameters and is independent of the surface ones, even though the field variance significantly depends also on surface parameters. In the latter case, the correlation time increases linearly with the surface correlation length and might reach quite large values, even in the case of dominating incoherent scattering.

Numerical results show that the proposed closed-form expressions of the correlation time are in excellent agreement with numerical simulations available in the literature for gently undulating surfaces, for which values as high as 300 ms have been obtained for a 100-m-altitude airborne GNSS-R. For high-altitude airborne GNSS-R, the received reflected signal remains correlated for time intervals as large as tens of ms, whereas for spaceborne receivers, correlation time is limited to few to several ms, according to the roughness regime. In addition, dependence of correlation time on roughness is stronger for airborne than for spaceborne systems. Finally, correlation time increases as the correlation length increases, and the rate decreases with increasing height standard deviation.

It must be noted that similar conclusions on the behavior of correlation time have been very recently obtained in [28]. However, at variance with our approach, the formulation of [28] does not lead to a closed-form expression of the correlation time, and it only holds if the receiver moves along the $x$-direction.

## Appendix A

The illumination function $w(x, y)$ and, hence, the system semiresolutions $A_x$ and $A_y$ are determined by the Woodward ambiguity function (WAF) [2] and, usually in a much lesser extent, by the receiver's antenna pattern. The shape of the illumination function may be irregular, depending on the observation geometry, but since only the region around its maximum is of interest, the assumption of a Gaussian shape is usually acceptable, especially if we are mainly interested in the correlation time, rather than in the exact behavior of the correlation coefficient. With reference to the resolution cell containing the specular point (i.e., the origin of our reference system), the semiresolutions along $x$ and $y$, appearing in (3), can be determined as follows:

$$\begin{aligned} A_x &= \min\{A_{xa}, A_{xp}, A_{xD}\} \\ A_y &= \min\{A_{ya}, A_{yp}, A_{yD}\} \end{aligned} \tag{44}$$

where:

$A_{xa}$ and $A_{ya}$ are the $x$ and $y$ half-sizes of the antenna ground footprint, i.e., the beam-limited semiresolutions;

$$A_{yp} \cong \sqrt{r_{R1}c}/B \text{ and } A_{xp} \cong A_{yp}/\cos\vartheta_0 \tag{45}$$

are the pulse-limited semiresolutions along $y$ and $x$, with $c$ being the speed of light and $B$ is the bandwidth of the transmitted signal;

$A_{xD}$ and $A_{yD}$ are the Doppler-limited semiresolutions along $x$ and $y$, which also depend in a rather involved way on incidence angle and receiver velocity direction, but are of the order of

$$A_{x,yD} \sim \lambda r_{R1}/(vt_{ci}) \tag{46}$$

with $t_{ci}$ being the coherent integration time [2].

In some applications, the Doppler processing is not performed, in which case, we can ignore $A_{xD}$ and $A_{yD}$ in (44) (i.e., we can let $A_{xD} \to \infty$ and $A_{yD} \to \infty$).

Some values of resolutions for the same GNSS-R systems of Table I and for different values of the incidence angle are reported in Table II. In Table II, also the glistening area sizes are reported, for surface roughness parameters typical of both sea surface, $\sigma/(a_0L) = 0.1$, and gently undulating soil, $\sigma/(a_0L) = 0.005$.

Numerical values of resolution in Table II show that $v\Delta t$ is much smaller than resolution up to time lags $\Delta t$ of the order of the hundreds of milliseconds. In addition, resolution is always much smaller than sensor distance, except for the low-altitude airborne receiver (and for incidence at low grazing angle).

With regard to the glistening area size, Table II shows that for sea surfaces, it is always greater than resolution, except for the low-altitude, low-velocity airborne sensor. Conversely, for gently undulating soils, it is always smaller than resolution, except for the spaceborne sensor, for which it is comparable with resolution. However, if we consider the lower value $\sigma/(a_0 L) = 0.001$, which is also reasonable (see Section III), and then, the glistening area size is smaller than resolution also for the spaceborne system. In general, the ratio of glistening area size and pulse-limited resolution is of the order of, see (23) and (45)

$$\frac{G_{x,y}}{A_{x,yp}} \sim \frac{4\sigma}{a_0 L}\sqrt{\frac{r_{R1}}{c/B}} \tag{47}$$

and the ratio of glistening area size and Doppler-limited resolution is of the order of, see (23) and (46)

$$\frac{G_{x,y}}{A_{x,yD}} \sim \frac{4\sigma}{a_0 L}\frac{v t_{ci}}{\lambda}. \tag{48}$$

These equations show that it is easier that $G_{x,y} < A_{x,y}$ (and hence, that correlation time depends on surface roughness) for low-altitude (47) and low-velocity (48) sensors, in agreement with some previous experimental and theoretical evidence [17].

## Appendix B

Let us consider the function

$$g(U,\Delta) = \exp\left\{-U^2[1-C(\Delta)]\right\} - \exp\left\{-U^2\right\} \tag{49}$$

which appears in (15), with $U = k\sigma u_z$ and $\Delta = \sqrt{\Delta x^2 + \Delta y^2}$, as well as in the expression of the scattered field variance for the KA and the SSA1 [29], [30]. We also assume that

$$C(0) = 1, \quad C'(0) = \left.\frac{dC}{d\Delta}\right|_{\Delta=0} = 0, \; C''(0) = \left.\frac{d^2C}{d\Delta^2}\right|_{\Delta=0} < 0.$$
$$C(\Delta) \cong 0 \text{ for } \Delta \gg L, \text{ and } C(\Delta) = 0. \tag{50}$$

It is easy to verify that the function $g(U, \Delta)$ has the following properties:

$$\text{for } U \gg 1 \quad g(U,\Delta) \cong \exp\left\{-\frac{U^2|C''(0)|}{2}\Delta^2\right\} \tag{51}$$

$$\text{for } U \ll 1 \quad g(U,\Delta) \cong U^2 C(\Delta) \tag{52}$$

$$\text{for } \Delta \gg L \quad g(U,\Delta) \ll \max\{g\} = 1 - \exp\left\{-U^2\right\} \tag{53}$$

$$\text{for } \Delta \ll L \quad g(U,\Delta) \cong 1 - \exp\left\{-U^2\right\} - \frac{U^2|C''(0)|}{2}\Delta^2. \tag{54}$$

Let us now consider the function

$$\tilde{g}(U,\Delta) = \left(1-\exp\left\{-U^2\right\}\right)\exp\left\{-\frac{U^2|C''(0)|}{2\left(1-\exp\left\{-U^2\right\}\right)}\Delta^2\right\}. \tag{55}$$

It is straightforward to verify that also this function satisfies properties (51), (53), and (54). Conversely, the property (52) is replaced by the following one:

$$\text{for } U \ll 1 \quad \tilde{g}(U,\Delta) \cong U^2 \exp\left\{-\frac{|C''(0)|}{2}\Delta^2\right\}. \tag{56}$$

If we consider the Gaussian autocorrelation function of (16), i.e.,

$$C(\Delta) = \exp\left(-\Delta^2/L^2\right) \tag{57}$$

then $C''(0) = -2/L^2$ and (56) coincides with (52). Therefore, it is reasonable to try to verify if, for Gaussian autocorrelation function, $\tilde{g}(U, \Delta)$ is a good approximation of $g(U, \Delta)$ for any value of $U$ and $\Delta$. Actually, this is the case, as illustrated in Fig. 7. In fact, Fig. 7 shows that the approximation is excellent for any $\Delta$ if $U \geq 3$ or $U \leq 0.5$; for intermediate values of $U$, it is excellent for small $\Delta$ and reasonably good for large $\Delta$.

In conclusion, for Gaussian autocorrelation function, $g(U, \Delta)$ can be approximated by $\tilde{g}(U, \Delta)$ for any value of $U$, and therefore, (15) can be approximated by (17). In addition, for large values of $U$ (i.e., of $k\sigma$), $g(U, \Delta)$ can be approximated by $\tilde{g}(U, \Delta)$ for any autocorrelation function since both are approximately given by (51); accordingly, (15) can be approximated by (19), provided that for non-Gaussian correlation function, $L^2$ is replaced by $2/|C''(0)|$.

## Appendix C

Here, we expand the argument of the last exponential function in (21) around the origin

$$\begin{aligned}\xi(x,y) &= \frac{1}{2}\frac{u_x^2(x,y)+u_y^2(x,y)}{2\frac{\sigma^2 u_z^2(x,y)}{L^2 a^2(x,y)}} \\ &= \frac{L^2}{4\sigma^2}\left\{\left[\frac{a(x,y)u_x(x,y)}{u_z(x,y)}\right]^2 + \left[\frac{a(x,y)u_y(x,y)}{u_z(x,y)}\right]^2\right\} \\ &\cong \left.\frac{\partial\xi}{\partial x}\right|_{\substack{x=0\\y=0}} x + \left.\frac{\partial\xi}{\partial y}\right|_{\substack{x=0\\y=0}} y + \frac{1}{2}\left.\frac{\partial^2\xi}{\partial x^2}\right|_{\substack{x=0\\y=0}} x^2 \\ &\quad + \left.\frac{\partial^2\xi}{\partial x\partial y}\right|_{\substack{x=0\\y=0}} xy + \frac{1}{2}\left.\frac{\partial^2\xi}{\partial y^2}\right|_{\substack{x=0\\y=0}} y^2.\end{aligned} \tag{58}$$

First of all, by keeping in mind that $u_x(0,0) = u_y(0,0) = 0$, we get

$$\left.\frac{\partial}{\partial p}\left(\frac{au_q}{u_z}\right)^2\right|_{\substack{x=0\\y=0}} = 2\left(\frac{au_q}{u_z}\right)\left.\frac{\partial}{\partial p}\left(\frac{au_q}{u_z}\right)\right|_{\substack{x=0\\y=0}} = 0 \tag{59}$$

where $p$ and $q$ may both stand for $x$ or $y$. Therefore, the first derivatives in (58) are equal to zero. In addition

$$\begin{aligned}&\left.\frac{\partial^2}{\partial p\partial q}\left(\frac{au_s}{u_z}\right)^2\right|_{\substack{x=0\\y=0}} \\ &= \left.\frac{\partial}{\partial p}\left[2\left(\frac{au_s}{u_z}\right)\frac{\partial}{\partial q}\left(\frac{au_s}{u_z}\right)\right]\right|_{\substack{x=0\\y=0}} \\ &= 2\left.\left[\frac{\partial}{\partial p}\left(\frac{au_s}{u_z}\right)\frac{\partial}{\partial q}\left(\frac{au_s}{u_z}\right) + \left(\frac{au_s}{u_z}\right)\frac{\partial^2}{\partial p\partial q}\left(\frac{au_s}{u_z}\right)\right]\right|_{\substack{x=0\\y=0}} \\ &= 2\left.\left[\frac{\partial}{\partial p}\left(\frac{au_s}{u_z}\right)\frac{\partial}{\partial q}\left(\frac{au_s}{u_z}\right)\right]\right|_{\substack{x=0\\y=0}}\end{aligned} \tag{60}$$

where $p$, $q$, and $s$ may all stand for $x$ or $y$. Finally,

$$\frac{\partial}{\partial p}\left(\frac{au_q}{u_z}\right)\Bigg|_{\substack{x=0\\y=0}} = \left[u_q\frac{\partial}{\partial p}\left(\frac{a}{u_z}\right)+\frac{a}{u_z}\frac{\partial u_q}{\partial p}\right]\Bigg|_{\substack{x=0\\y=0}} = \frac{a}{u_z}\frac{\partial u_q}{\partial p}\Bigg|_{\substack{x=0\\y=0}}. \tag{61}$$

Therefore, in order to compute the second derivatives in (60), we only need to evaluate the following derivatives:

$$\frac{\partial u_x}{\partial x}\Bigg|_{\substack{x=0\\y=0}} = \frac{\partial^2(R_T+R_{R1})}{\partial x^2}\Bigg|_{\substack{x=0\\y=0}} = \frac{1}{r_T}\left(1-\frac{|x_T|^2}{r_T^2}\right)+\frac{1}{r_{R1}}\left(1-\frac{x_{R1}^2}{r_{R1}^2}\right) = \frac{r_T+r_{R1}}{r_T r_{R1}}\cos^2\vartheta_0 \tag{62}$$

$$\frac{\partial u_y}{\partial y}\Bigg|_{\substack{x=0\\y=0}} = \frac{\partial^2(R_T+R_{R1})}{\partial y^2}\Bigg|_{\substack{x=0\\y=0}} = \frac{1}{r_T}+\frac{1}{r_{R1}} = \frac{r_T+r_{R1}}{r_T r_{R1}} \tag{63}$$

$$\frac{\partial u_x}{\partial y}\Bigg|_{\substack{x=0\\y=0}} = \frac{\partial u_y}{\partial x}\Bigg|_{\substack{x=0\\y=0}} = \frac{\partial^2(R_T+R_{R1})}{\partial x\partial y}\Bigg|_{\substack{x=0\\y=0}} = 0 \tag{64}$$

where use has been made of (14).

Replacing (59)–(64) in (58), we get

$$\frac{1}{2}\frac{u_x^2(x,y)+u_y^2(x,y)}{2\frac{\sigma^2u_z^2(x,y)}{L^2a^2(x,y)}} \cong \frac{1}{4}\frac{L^2a_0^2}{4\sigma^2}\left(\frac{r_T+r_{R1}}{r_T r_{R1}}\right)^2\cos^2\vartheta_0 x^2 + \frac{1}{4}\frac{L^2a_0^2}{4\sigma^2\cos^2\vartheta_0}\left(\frac{r_T+r_{R1}}{r_T r_{R1}}\right)^2 y^2 \tag{65}$$

which leads to (22)–(23).

## Appendix D

In this appendix, we recall some useful mathematical relations that have been used in Section II. First of all, the FT of a Gaussian function is

$$\int_{-\infty}^{+\infty}\frac{1}{\sqrt{2\pi}\,\Sigma}\exp\left(-\frac{\xi^2}{2\Sigma^2}\right)\exp(j\omega\xi)d\xi = \exp\left(-\frac{\omega^2\Sigma^2}{2}\right). \tag{66}$$

If $\xi$ is a zero-mean Gaussian random variable with standard deviation $\Sigma$, then (66) can also be read as the statistical mean of $\exp(j\omega\xi)$, i.e., characteristic function of $\xi$ [32]

$$\langle\exp(j\omega\xi)\rangle = \exp\left(-\frac{\omega^2\Sigma^2}{2}\right). \tag{67}$$

Equation (12) is obtained by using (67) with $\omega = k$ and

$$\begin{aligned}
\xi &= u_{z1}(x,y)z(x,y) - u_{z2}(x',y')z(x',y'), \text{ so that}\\
\Sigma^2 &= \left\langle\left(u_{z1}(x,y)z(x,y) - u_{z2}(x',y')z(x',y')\right)^2\right\rangle\\
&= \sigma^2\left[u_{z1}^2(x,y)+u_{z2}^2(x',y') - 2u_{z1}(x,y)u_{z2}(x',y')C(\Delta x,\Delta y)\right];\\
\xi &= u_{z1}(x,y)z(x,y), \text{ so that}\\
\Sigma^2 &= \left\langle(u_{z1}(x,y)z(x,y))^2\right\rangle = \sigma^2u_{z1}^2(x,y);\\
\text{and } \xi &= u_{z2}(x',y')z(x',y'), \text{ so that}\\
\Sigma^2 &= \left\langle\left(u_{z2}(x',y')z(x',y')\right)^2\right\rangle = \sigma^2u_{z2}^2(x',y').
\end{aligned}$$

## References


[1] C. Zuffada, T. Elfouhaily, and S. Lowe, "Sensitivity analysis of wind vector measurements from ocean reflected GPS signals," *Remote Sens. Environ.*, vol. 88, no. 3, pp. 341–350, Dec. 2003.

[2] V. U. Zavorotny, S. Gleason, E. Cardellach, and A. Camps, "Tutorial on remote sensing using GNSS bistatic radar of opportunity," *IEEE Geosci. Remote Sens. Mag.*, vol. 2, no. 4, pp. 8–45, Dec. 2014.

[3] C. S. Ruf, S. Gleason, and D. S. McKague, "Assessment of CYGNSS wind speed retrieval uncertainty," *IEEE J. Sel. Topics Appl. Earth Observ. Remote Sens.*, vol. 12, no. 1, pp. 87–97, Jan. 2019.

[4] J. Reynolds, M. P. Clarizia, and E. Santi, "Wind speed estimation from CYGNSS using artificial neural networks," *IEEE J. Sel. Topics Appl. Earth Observ. Remote Sens.*, vol. 13, pp. 708–716, 2020.

[5] M. P. Clarizia and C. S. Ruf, "Statistical derivation of wind speeds from CYGNSS data," *IEEE Trans. Geosci. Remote Sens.*, vol. 58, no. 6, pp. 3955–3964, Jun. 2020.

[6] M. M. Al-Khaldi, A. Bringer, and J. T. Johnson, "Studies of a rapid change detector using CYGNSS level-2 wind speed products," *IEEE J. Sel. Topics Appl. Earth Observ. Remote Sens.*, vol. 14, pp. 7931–7937, 2021.

[7] W. Guo, H. Du, J. W. Cheong, B. J. Southwell, and A. G. Dempster, "GNSS-R wind speed retrieval of sea surface based on particle swarm optimization algorithm," *IEEE Trans. Geosci. Remote Sens.*, vol. 60, pp. 1–14, 2022, 4202414.

[8] H. Carreno-Luengo, G. Luzi, and M. Crosetto, "First evaluation of topography on GNSS-R: An empirical study based on a digital elevation model," *Remote Sens.*, vol. 11, no. 21, p. 2556, Oct. 2019.

[9] H. Carreno-Luengo, G. Luzi, and M. Crosetto, "Sensitivity of CyGNSS bistatic reflectivity and SMAP microwave radiometry brightness temperature to geophysical parameters over land surfaces," *IEEE J. Sel. Topics Appl. Earth Observ. Remote Sens.*, vol. 12, no. 1, pp. 107–122, Jan. 2019.

[10] M. P. Clarizia, N. Pierdicca, F. Costantini, and N. Floury, "Analysis of CYGNSS data for soil moisture retrieval," *IEEE J. Sel. Topics Appl. Earth Observ. Remote Sens.*, vol. 12, no. 7, pp. 2227–2235, Jul. 2019.

[11] A. M. Balakhder, M. M. Al-Khaldi, and J. T. Johnson, "On the coherency of ocean and land surface specular scattering for GNSS-R and signals of opportunity systems," *IEEE Trans. Geosci. Remote Sens.*, vol. 57, no. 12, pp. 10426–10436, Dec. 2019.

[12] D. Comite and N. Pierdicca, "Decorrelation of the near-specular land scattering in bistatic radar systems," *IEEE Trans. Geosci. Remote Sens.*, vol. 60, pp. 1–13, 2022.

[13] A. Bringer, J. T. Johnson, C. Toth, C. Ruf, and M. Moghaddam, "Studies of terrain surface roughness and its effect on GNSS-R systems using airborne lidar measurements," in *Proc. IEEE Int. Geosci. Remote Sens. Symp. (IGARSS)*, Jul. 2021, pp. 2016–2019.

[14] M. Born and E. Wolf, *Principles of Optics*. Oxford, U.K.: Pergamon Press, 1980.

[15] H. A. Zebker and J. Villasenor, "Decorrelation in interferometric radar echoes," *IEEE Trans. Geosci. Remote Sens.*, vol. 30, no. 5, pp. 950–959, Sep. 1992.

[16] G. Franceschetti, A. Iodice, M. Migliaccio, and D. Riccio, "The effect of surface scattering on IFSAR baseline decorrelation," *J. Electromagn. Waves Appl.*, vol. 11, no. 3, pp. 353–370, Jan. 1997.

[17] H. You, J. L. Garrison, G. Heckler, and D. Smajlovic, "The autocorrelation of waveforms generated from ocean-scattered GPS signals," *IEEE Geosci. Remote Sens. Lett.*, vol. 3, no. 1, pp. 78–82, Jan. 2006.
[18] H. You, G. Heckler, J. L. Garrison, and V. U. Zavorotny, "Stochastic voltage model and experimental measurement of ocean-scattered GPS signal statistics," *IEEE Trans. Geosci. Remote Sens.*, vol. 42, no. 10, pp. 2160–2169, Oct. 2004.
[19] M. Martin-Neira, S. D'Addio, C. Buck, N. Floury, and R. Prieto-Cerdeira, "The Paris ocean altimeter in-orbit demonstrator," *IEEE Trans. Geosci. Remote Sens.*, vol. 49, no. 6, pp. 2209–2237, Jun. 2011.
[20] J. L. Garrison, "A statistical model and simulator for ocean-reflected GNSS signals," *IEEE Trans. Geosci. Remote Sens.*, vol. 54, no. 10, pp. 6007–6019, Oct. 2016.
[21] W. Li, A. Rius, F. Fabra, E. Cardellach, S. Ribó, and M. Martín-Neira, "Revisiting the GNSS-R waveform statistics and its impact on altimetric retrievals," *IEEE Trans. Geosci. Remote Sens.*, vol. 56, no. 5, pp. 2854–2871, May 2018.
[22] A. Calabia, I. Molina, and S. Jin, "Soil moisture content from GNSS reflectometry using dielectric permittivity from Fresnel reflection coefficients," *Remote Sens.*, vol. 12, no. 1, p. 122, 2020.
[23] S. H. Yueh, R. Shah, M. J. Chaubell, A. Hayashi, X. Xu, and A. Colliander, "A semiempirical modeling of soil moisture, vegetation, and surface roughness impact on CYGNSS reflectometry data," *IEEE Trans. Geosci. Remote Sens.*, vol. 60, 2022, Art. no. 5800117.
[24] Y. Wang and Y. J. Morton, "Coherent GNSS reflection signal processing for high-precision and high-resolution spaceborne applications," *IEEE Trans. Geosci. Remote Sens.*, vol. 59, no. 1, pp. 831–842, Jan. 2021.
[25] E. Loria, A. O'Brien, V. Zavorotny, B. Downs, and C. Zuffada, "Analysis of scattering characteristics from inland bodies of water observed by CYGNSS," *Remote Sens. Environ.*, vol. 245, Aug. 2020, Art. no. 111825.
[26] A. Egido *et al.*, "Airborne GNSS-R polarimetric measurements for soil moisture and above-ground biomass estimation," *IEEE J. Sel. Topics Appl. Earth Observ. Remote Sens.*, vol. 7, no. 5, pp. 1522–1532, May 2014.
[27] M. M. Al-Khaldi *et al.*, "Inland water body mapping using CYGNSS coherence detection," *IEEE Trans. Geosci. Remote Sens.*, vol. 59, no. 9, pp. 7385–7394, Sep. 2021.
[28] D. Comite and N. Pierdicca, "Decorrelation of the near-specular scattering in GNSS reflectometry from space," *IEEE Trans. Geosci. Remote Sens.*, vol. 60, pp. 1–13, 2022.
[29] F. T. Ulaby, R. K. Moore, and A. K. Fung, *Microwave Remote Sensing*, vol. 2. Reading, MA, USA: Artech House, 1982.
[30] A. G. Voronovich, "Small-slope approximation for electromagnetic wave scattering at a rough interface of two dielectric half-spaces," *Waves Random Media*, vol. 4, no. 3, pp. 337–367, Jul. 1994.
[31] S. Principe, T. Beltramonte, M. di Bisceglie, and C. Galdi, "GNSS ocean bistatic statistical scattering in the time-varying regime: Modeling and correlation properties," *IEEE Trans. Geosci. Remote Sens.*, vol. 60, pp. 1–8, 2022.
[32] A. Papoulis, *Probability, Random Variables, and Stochastic Processes*, 3rd ed. New York, NY, USA: McGraw-Hill, 1991.
[33] D. Comite, F. Ticconi, L. Dente, L. Guerriero, and N. Pierdicca, "Bistatic coherent scattering from rough soils with application to GNSS reflectometry," *IEEE Trans. Geosci. Remote Sens.*, vol. 58, no. 1, pp. 612–625, Jan. 2020.
[34] L. Dente, L. Guerriero, D. Comite, and N. Pierdicca, "Space-borne GNSS-R signal over a complex topography: Modeling and validation," *IEEE J. Sel. Topics Appl. Earth Observ. Remote Sens.*, vol. 13, pp. 1218–1233, 2020.
[35] O. Nogues-Correig, E. Cardellach Gali, J. Sanz Campderros, and A. Rius, "A GPS-reflections receiver that computes Doppler/delay maps in real time," *IEEE Trans. Geosci. Remote Sens.*, vol. 45, no. 1, pp. 156–174, Jan. 2007.
[36] M. Unwin, P. Jales, J. Tye, C. Gommenginger, G. Foti, and J. Rosello, "Spaceborne GNSS-reflectometry on TechDemoSat-1: Early mission operations and exploitation," *IEEE J. Sel. Topics Appl. Earth Observ. Remote Sens.*, vol. 9, no. 10, pp. 4525–4539, Oct. 2016.
[37] G. Franceschetti, A. Iodice, M. Migliaccio, and D. Riccio, "Scattering from natural rough surfaces modelled by fractional Brownian motion two-dimensional processes," *IEEE Trans. Anten. Propag.*, vol. 47, no. 9, pp. 1405–1415, Sep. 1999.

**Gerardo Di Martino** (Senior Member, IEEE) was born in Naples, Italy, in 1979. He received the Laurea degree (*cum laude*) in telecommunication engineering and the Ph.D. degree in electronic and telecommunication engineering from the University of Naples Federico II, Naples, in 2005 and 2009, respectively.

From 2009 to 2016, he was with the University of Naples Federico II, working on projects regarding applied electromagnetics and remote sensing topics. From 2014 to 2015, he was with the Italian National Consortium for Telecommunications (CNIT), Naples, Italy, and in 2016, he was with the Regional Center Information Communication Technology (CeRICT), Naples. He is currently a tenure-track Assistant Professor of Electromagnetics with the Department of Electrical Engineering and Information Technology, University of Naples Federico II. His research interests include microwave remote sensing and electromagnetics, with a focus on electromagnetic scattering from natural surfaces and urban areas, synthetic aperture radar (SAR) signal processing and simulation, information retrieval from SAR data, and electromagnetic propagation in urban areas.

Dr. Di Martino is an Associate Editor of IEEE JOURNAL OF SELECTED TOPICS ON APPLIED EARTH OBSERVATIONS AND REMOTE SENSING, IEEE ACCESS, *Remote Sensing* (MDPI), and *Electronics* (MDPI).

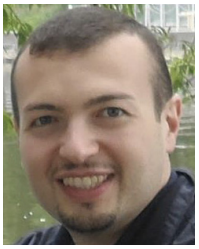

**Alessio Di Simone** (Member, IEEE) was born in Torre del Greco, Italy, in 1989. He received the B.Sc. and M.Sc. Laurea degrees (*cum laude*) in telecommunication engineering and the Ph.D. degree in information technology and electrical engineering from the University of Naples Federico II, Naples, Italy, in 2011, 2013, and 2017, respectively.

In 2016, he joined the Universitat Politècnica de Catalunya, Barcelona, Spain, as a Visiting Researcher. In 2017 and 2018, he joined the NATO Science and Technology Organization Centre for Maritime Research and Experimentation (CMRE), La Spezia, Italy, as a Visiting Researcher. Since 2017, he has been a Research Fellow with the Department of Information Technology and Electrical Engineering, University of Naples Federico II. His main research interests are in the field of microwave remote sensing and electromagnetics including modeling of the electromagnetic scattering from natural surfaces, urban areas, and artificial targets, and simulation and processing of synthetic aperture radar (SAR) and Global Navigation Satellite System Reflectometry (GNSS-R) data.

Dr. Di Simone was awarded a prize for the Best Master Thesis in Remote Sensing by the IEEE South Italy Geoscience and Remote Sensing Chapter in 2015.

**Antonio Iodice** (Senior Member, IEEE) was born in Naples, Italy, in 1968. He received the Laurea degree (*cum laude)* in electronic engineering and the Ph.D. degree in electronic engineering and computer science from the University of Naples Federico II, Naples, in 1993 and 1999, respectively.

In 1995, he joined the Research Institute for Electromagnetism and Electronic Components of the Italian National Council of Research (IRECE-CNR), Naples. From 1999 to 2000, he was with Telespazio S.p.A., Rome, Italy. He was a Research Scientist with the University of Naples Federico II from 2000 to 2004, where he was a Professor of Electromagnetics from 2005 to 2018 and is currently a Full Professor of Electromagnetics with the Department of Electrical Engineering and Information Technology. He has been involved as a Principal Investigator or a Co-Investigator in several projects funded by European Union (EU), Italian Space Agency (ASI), Italian Ministry of Education and Research (MIUR), Campania Regional Government, and private companies. He has authored or coauthored more than 300 articles, of which over 100 published on refereed journals. His main research interests are in the field of microwave remote sensing and electromagnetics: modeling of electromagnetic scattering from natural surfaces and urban areas, simulation and processing of synthetic aperture radar (SAR) signals, and electromagnetic propagation in urban areas.

Prof. Iodice received the "2009 Sergei A. Schelkunoff Transactions Prize Paper Award" from the IEEE Antennas and Propagation Society, for the best paper published in 2008 on the IEEE TRANSACTIONS ON ANTENNAS AND PROPAGATION. He was recognized by the IEEE Geoscience and Remote Sensing Society as a 2015 Best Reviewer of the IEEE TRANSACTIONS ON GEOSCIENCE AND REMOTE SENSING. He is the Chair of the IEEE South Italy Geoscience and Remote Sensing Chapter.